Journal of Materials Chemistry A

ROYAL SOCIETY OF CHEMISTRY

COMMUNICATION

View Article Online
View Journal | View Issue

Cite this: J. Mater. Chem. A, 2022, 10, 19618

Received 21st March 2022
Accepted 24th May 2022

DOI: 10.1039/d2ta02245a

rsc.li/materials-a

Alloying Sb into all inorganic lead-free $CsBi_3I_{10}$ for improving the crystal growth and photovoltaic performance†

Jian Kang,[a] Shan Chen,*[b] Mengmeng Hao,[d] Junxian Liu,[a] Mohammad Al-Mamun,[a] Porun Liu,[a] Yun Wang,[a] Huajie Yin*[c] and Huijun Zhao*[a]

The all-inorganic lead-free perovskite $CsBi_3I_{10}$ has recently emerged as a promising light absorber. However, the poor morphology of $CsBi_3I_{10}$ film remains a critical issue for fabricating high-performance solar cells. In this work, we report an ion substitution strategy by alloying Sb into $CsBi_3I_{10}$, resulting in dramatically improved grain crystallinity and markedly reduced bandgaps for better light utilization. The Sb-substituted $CsBi_3I_{10}$ film composed of highly-crystalline large grains can form a bulk-heterojunction structure with the electron acceptor PCBM to facilitate the exciton separation. With PTAA as the hole transport layer, the solar cell assembled using $Cs(Bi_{0.7}Sb_{0.3})_3I_{10}$ can afford a champion power conversion efficiency of 1.54% with a high V_{oc} of 0.81 V.

[a]Centre for Catalysis and Clean Energy, School of Environment and Science, Griffith University, Gold Coast, QLD 4222, Australia. E-mail: h.zhao@griffith.edu.au

[b]Institutes of Physical Science and Information Technology, Anhui University, Hefei, 230039, China. E-mail: chenshan@ahu.edu.cn

[c]Institute of Solid-State Physics, Chinese Academy of Sciences, Hefei, 230031, China. E-mail: yinhj@issp.ac.cn

[d]School of Chemical Engineering, Australian Institute of Bioengineering and Nanotechnology, The University of Queensland, Brisbane, QLD 4072, Australia

† Electronic supplementary information (ESI) available. See https://doi.org/10.1039/d2ta02245a

Huajie Yin currently holds a Professor position at the Institute of Solid State Physics, Chinese Academy of Sciences. He obtained his PhD in 2015 from National centre for Nanoscience and Technology, and Tsinghua University, China. He subsequently took a Research Fellow position at the Centre for Clean Environment and Energy, Griffith University. His research is focused on controllable synthesis of 2D materials and the related applications in electrocatalysis, photocatalysis, energy storage and conversion.

Over the past decade, the lead-based halide perovskite solar cells have rapidly advanced to attain >25% efficiency.[1,2] Nevertheless, the presence of toxic lead is one of the major concerns for its commercialization.[3] The quest for non-toxic alternatives hence becomes increasingly urgent and many attempts have been made to explore lead-free perovskite materials for solar cell applications. Generally, highly efficient and defect-tolerant light absorbers such as lead-based halide perovskites require certain features, including small effective mass, larger dielectric constant, high band dispersion level, and valence band maximum with antibonding states.[4] In this regard, materials containing metal cations with ns^2 valence electrons, such as Sn^{2+}, Ge^{2+}, Sb^{3+}, and Bi^{3+}, exhibit most of these properties.[5–9] Among these lead-free perovskites, the interest in Bi-based halide perovskite derivatives has continued to increase due to their great potential to address both toxicity and instability issues.[5,6,10–12] However, Bi substitution usually leads to large bandgaps, low electronic dimensionality, and poor film quality, limiting the performance of Bi-based perovskite solar cells.[13,14]

Recently, a new type of Bi-based perovskite with the formula of ABi_3I_{10} ($A = Cs^+$, MA^+) has been explored as a promising candidate due to its intriguing optoelectronic properties, especially the suitable bandgap of ~1.77 eV.[15–17] In 2016, Johansson's group firstly reported the $CsBi_3I_{10}$ perovskite and its photovoltaic application in the meso-structured device, for which the photocurrent is still observable up to 700 nm and a power conversion efficiency (PCE) of 0.4% was achieved.[15] Later, several groups have focused their studies on enhancing the PCEs of $CsBi_3I_{10}$ solar cells *via* improving the film morphologies by adopting various strategies such as composition tuning,[18] solvent engineering,[19–23] and interface engineering.[24] For example, very recently, Zhang's group reported a gas quenching assisted antisolvent method combined with introducing a thiourea Lewis base additive to engineer the film microstructure.[22] However, the most reported PCEs of $CsBi_3I_{10}$ solar cells developed using the above-mentioned strategies are around 1% due to suboptimal morphology control. Achieving a high-quality thin film with large crystal grains, uniform coverage and smooth surface remains a big challenge for the

$CsBi_3I_{10}$ perovskite, due to its rapid crystallization rate.[16,18–22,24–26] It is therefore necessary to explore new strategies capable of modulating the crystallization kinetics (retarding the crystallization rate), to improve the film quality and photovoltaic performance of $CsBi_3I_{10}$.

On the other hand, ion substitution by incorporating appropriate ions into the host lattices has been proven to be an effective strategy to tailor the optoelectronic properties (such as bandgaps, trap states, and charge transport) of various perovskite materials.[27–34,38–41] For example, Kanatzidis's group alloyed the Sn^{2+} into $MAPbI_3$, achieving a narrowed bandgap of <1.3 eV and extending the photoresponse to the infrared region (up to 1050 nm) for the solid solution of $MASn_{1-x}Pb_xI_3$.[35] Notably, the suitable ion substitution can also improve the film morphology of perovskites.[31,36,37] For example, Mn^{2+} ion substituted all-inorganic perovskites $CsPb_{1-x}Mn_xI_{1+2x}Br_{2-2x}$ thin film, reported by Qi's group, showed better crystallinity and morphology than its undoped counterpart with enhanced photovoltaic performance.[31] However, to the best of our knowledge, the ion substitution strategy has yet been applied for the $CsBi_3I_{10}$ system.

In this work, we incorporate the isovalent Sb^{3+} into the $CsBi_3I_{10}$ perovskite to investigate the crystallization process and film growth of the solid solution of $Cs(Bi_{1-x}Sb_x)_3I_{10}$ ($x = 0$ to 0.5) and its photovoltaic performance. Alloying Sb^{3+} can efficiently retard the crystallization rate of $CsBi_3I_{10}$ perovskite, resulting in a thin film with higher crystallinity and larger grains. The film with an optimal composition of $Cs(Bi_{0.7}Sb_{0.3})_3I_{10}$ possessing evenly distributed single-layer and large crystal grains is utilized to construct a bulk-heterojunction structure with [6,6]-phenyl-C61-butyric acid methyl ester (PCBM) electron acceptor to promote the dissociation of excitons. After the optimization of the interface layer, the best performed solar cell achieves a champion PCE of 1.54% with excellent reproductivity.

The effect of Sb-substitution on the crystallization process and film morphology of $CsBi_3I_{10}$ (denoted as CBI) film is firstly investigated. As shown in the upper panel of Fig. 1a, the colour of spin-coated CBI film from a mixture solvent of DMF and DMSO (9 : 1 v/v) turns to black-brown in less than 30 s upon the thermal annealing treatment at 100 °C, indicating a rapid crystallization process. This rapid crystallization phenomenon for Bi-based perovskites is likely due to the much lower solubility of BiI_3 precursor and its weaker coordinating strength with the common Lewis base solvents.[38,39] The surface scanning electron microscope (SEM) image (Fig. 1b) indicates that the pristine CBI film is mostly consisted of randomly-oriented ultrasmall nanoparticles, due to the fast solvent evaporation during thermal annealing. The Sb^{3+}-substituted CBI films show distinct crystallization behaviour and film morphology. In contrast, the as-obtained spin-coated $Cs(Bi_{0.7}Sb_{0.3})_3I_{10}$ (denoted as CBSI-3) film takes ~60 s to fully change the colour from orange to black-brown under the same treatment conditions (Fig. 1a lower panel), reflecting the prolonged crystallization process of the solid solution film. All of the films with Sb-substitution show the similar slowed crystallization trend regardless of substitution ratio. The retarded crystallization might be caused by a stronger coordination of Sb^{3+} with the Lewis base solvent DMF or DMSO (solvent effect will be discussed in the following part). As shown in Fig. 1c and d and Fig. S1,† the Sb^{3+}-substituted CBI films are consisted of highly-crystallized thick nanoplates with sizes of up to several hundreds of nanometres. The CBSI-3 film with 30 mol% Sb substitution stands out in terms of uniformity, crystallinity, and crystal orientation. Further increasing the substitution ratio ($x \geq 0.5$), the film coverage is dramatically reduced probably because of low vaporization temperature of SbI_3.[40] Unlike the Pb-based perovskites that predominantly generate free charge carriers upon light absorption due to low exciton binding energy of 19–50 meV, Bi/Sb-based perovskites possess high exciton binding energy exceeding 200 meV and usually generate stable excitons.[33,42] The CBSI-3 film possesses evenly distributed nanoplates structure that are surrounded with continuous 200 nm-wide gaps (Fig. S2†). This specific morphology is favourable to construct bulk-heterojunction structure when combined with suitable electron acceptors, which can efficiently address the exciton separation issue of Bi-based perovskites.[43]

Fig. 1e and S3† show the X-ray diffraction (XRD) patterns of $Cs(Bi_{1-x}Sb_x)_3I_{10}$ ($x = 0$ to 0.5) films deposited on the PEDOT substrates. From the pristine CBI to the $Cs(Bi_{0.5}Sb_{0.5})_3I_{10}$ (denoted as CBSI-5) with increasing the Sb-substitution ratio, the main diffraction peak shifts slightly from 12.85° to 13.05° (Fig. S3b†). The slight shift to higher angels of the main peak can be attributed to the smaller ionic radius of the Sb^{3+} cation than that of Bi^{3+}, indicating a small change in the lattice parameters and complete mixing of the solid solution. No new peaks appear means no phase transition occurred for all of the $Cs(Bi_{1-x}Sb_x)_3I_{10}$ thin films even at high substitution ratio ($x = 0.5$). Among these films, the film with $x = 0.3$ owns the highest peak intensity (Fig. 1e and S3a†), which states the best crystallization of CBSI-3 film and agrees with SEM results. The presence of the peak at ~13° can be assigned to the (003) plane, indicating the preferred crystal growth along the *c*-axis.

The Sb-substitution effect on the surface chemistry of CBI thin films is studied by X-ray photo-electron spectroscopy (XPS). High resolution spectra of Cs 3d, Bi 4f, I 3d, and Sb 3d of the pristine CBI and/or CBSI-3 films are shown in Fig. 2a–d. These two films unveil identical peaks of Cs 3d, Bi 4f and I 3d electronic states, indicating that the Sb-substituted CBSI-3 thin film maintains the similar electronic structure with CBI film. In Fig. 2d, the peaks of CBSI-3 thin film located at 530.4 eV and 539.7 eV correspond to the binding energies of Sb^{3+} $3d_{5/2}$ and Sb^{3+} $3d_{3/2}$, and the peak at 532.5 eV corresponds to O 1s.[43] These indicate the presence of antimony in its trivalent form in the solid solution.[43,44] Fig. 2e and S4† show the absorption spectra of $Cs(Bi_{1-x}Sb_x)_3I_{10}$ thin films ($x = 0$ to 0.5). The bandgaps of these films reduce with the Sb contents increasing, consistent with the previous study on $MA_3(Bi_{1-x}Sb_x)_2I_9$ system.[32,43] The calculated direct (indirect) bandgaps are reduced from 1.88 eV (1.82 eV) for CBI to 1.66 eV (1.57 eV) for CBSI-5 as shown in Fig. S5–S7.† The CBSI-3 film possesses the direct and indirect bandgaps of 1.79 eV and 1.72 eV, respectively. The reduced bandgap of active layer could lead to the widened absorption and the better utilization of light energy.

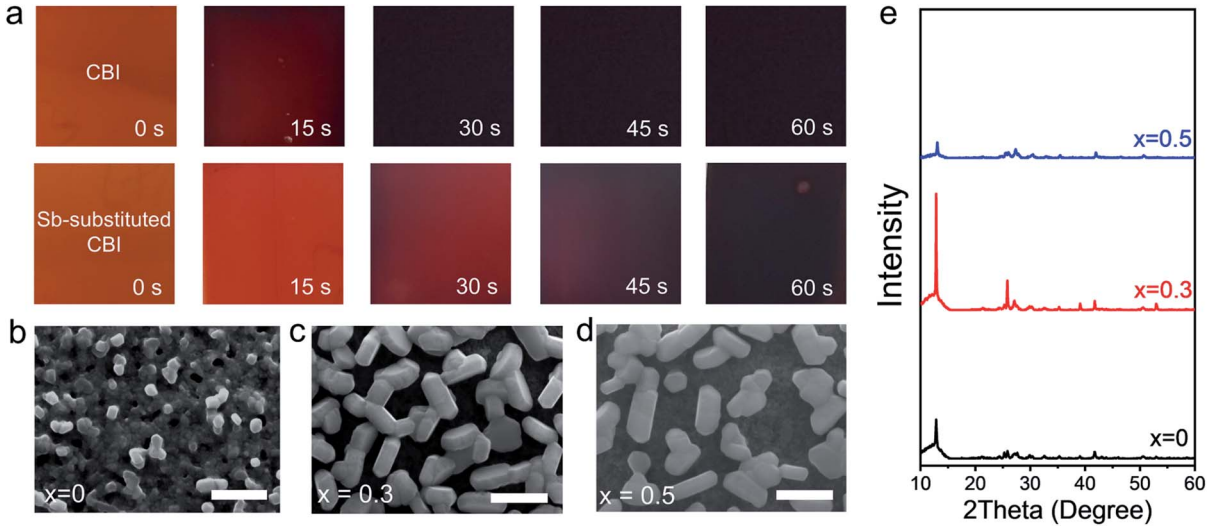

Fig. 1 (a) Photographs of $CsBi_3I_{10}$ (CBI) and $Cs(Bi_{0.7}Sb_{0.3})_3I_{10}$ (CBSI-3) films with different thermal annealing duration. SEM images of (b) CBI, (c) CBSI-3, and (d) CBSI-5 films, the scale bar corresponds to 500 nm. (e) XRD patterns of CBI ($x = 0$), CBSI-3 ($x = 0.3$), and CBSI-5 ($x = 0.5$) films. (All films illustrated here are synthesized from DMF/DMSO mixed solvent with the volume ratio of 9 : 1).

The Sb-substitution effect on the photovoltaic performance of CBI films is then evaluated by fabricating solar cells with an inverted device architecture (ITO/PEDOT/$Cs(Bi_{1-x}Sb_x)_3I_{10}$/PCBM/BCP/Ag). All films discussed here are synthesized from DMF/DMSO mixed solvent with volume ratio of 9 : 1. As shown in Fig. 2f, the CBSI-3 based solar cells exhibit obvious enhancement for the PCE (0.62%) and the open-circuit voltage (V_{oc}, 0.74 V), compared with those (0.45% PCE and 0.47 V V_{oc}) of the pristine CBI based solar cells (Table S1†). The short-circuit current density (J_{sc}) almost remain the same for CBI and CBSI-3 based devices. The improved performance of CBSI-3 is mainly attributed to the improved crystallinity of perovskite grain. The CBSI-5 based devices perform poorly, possibly due to its low film coverage. This preliminary photovoltaic evaluation combined with the above characterizations indicate that the CBSI-3 possesses the best composition with 30 mol% Sb^{3+} substitution, which will be adopted in the following study of solvent effect.

The solvent effect on the film growth and the photovoltaic performance is investigated by fabricating CBSI-3 films from 11 solvents with DMSO concentrations of 0% to 100% (10% interval), considering that the retarded crystallization is possibly caused by the stronger coordination between Lewis acid Sb^{3+} and Lewis base solvent. The UV-vis spectra (Fig. 3a) show the absorption intensity, especially in the 550–800 nm region, gradually increases when increasing the volume ratio of DMSO. SEM images (Fig. 3b, S8 and S9†) show that the introduction of DMSO plays a vital role in promoting the crystal grain growth. The CBSI-3 film synthesized from the pure DMF (DMSO = 0 vol%) is almost amorphous as evidenced by the extremely low-intensity XRD peaks shown in Fig. S10,† while the CBSI-3 films synthesized from DMF/DMSO mixed solvents show distinctive morphologies with large crystal grains sized around several hundreds of nanometres, regardless of the volume ratio of DMSO. The Lewis basicity of the solvents can be quantified by Gutmann's donor number D_N, which indicates the coordinating strength of Lewis acid–base complex.[45,46] Loo *et al.* reported that high D_N solvent such as DMSO coordinates more strongly with the Pb^{2+} centre, which in turn inhibits iodide coordination and stalls $MAPbI_3$ perovskite crystallization.[45] Here, the higher D_N (30.0 kcal mol^{-1}) solvent DMSO (compared to DMF with a D_N of 26.6 kcal mol^{-1}) might form a stronger coordination strength with Sb^{3+} centres, which slows down the CBSI perovskite crystallization and enlarges the grains. It is also notable that the crystal nanoplates for films synthesized from the high DMSO-concentration solvents are single-layered and more separated instead of overlapping or over-aggregating. For the Bi-based perovskites with high exciton binding energy, the separated grains can increase the interfacial contact area between CBSI and PCBM electron acceptor, facilitating the efficient exciton separation and charge transfer, while the aggregated grains might raise more possibilities for recombination at the grain boundaries (Fig. 3c). Steady-state and time-resolved photoluminescence (PL) were investigated for CSBI-3 films prepared from low-DMSO-contained and high-DMSO-contained solvents, respectively (Fig. S11†). The stronger PL peak intensity (Fig. S11a†) and longer PL lifetime (Fig. S11b†) of film from high-DMSO-contained solvent (100 vol%) indicate the supressed non-radiative recombination in this film and verify the proposed mechanism in Fig. 3c. The photovoltaic performances of CBSI-3 films synthesized from the mixed solvents with different DMSO volume ratios are studied. Fig. 3d and S12† show the corresponding current density–voltage (J–V) curves. The performance of CBSI-3 is enhanced with the increased DMSO volume ratio, which agrees with the UV-vis absorption and morphological results. The device based on CBSI-3 film synthesized by using 100 vol% DMSO as solvent yields a highest PCE of 1.06% (V_{oc} = 0.75 V, J_{sc} = 4.62 mA cm^{-2}, and fill factor (FF) = 30.7%) under the same experimental conditions. The

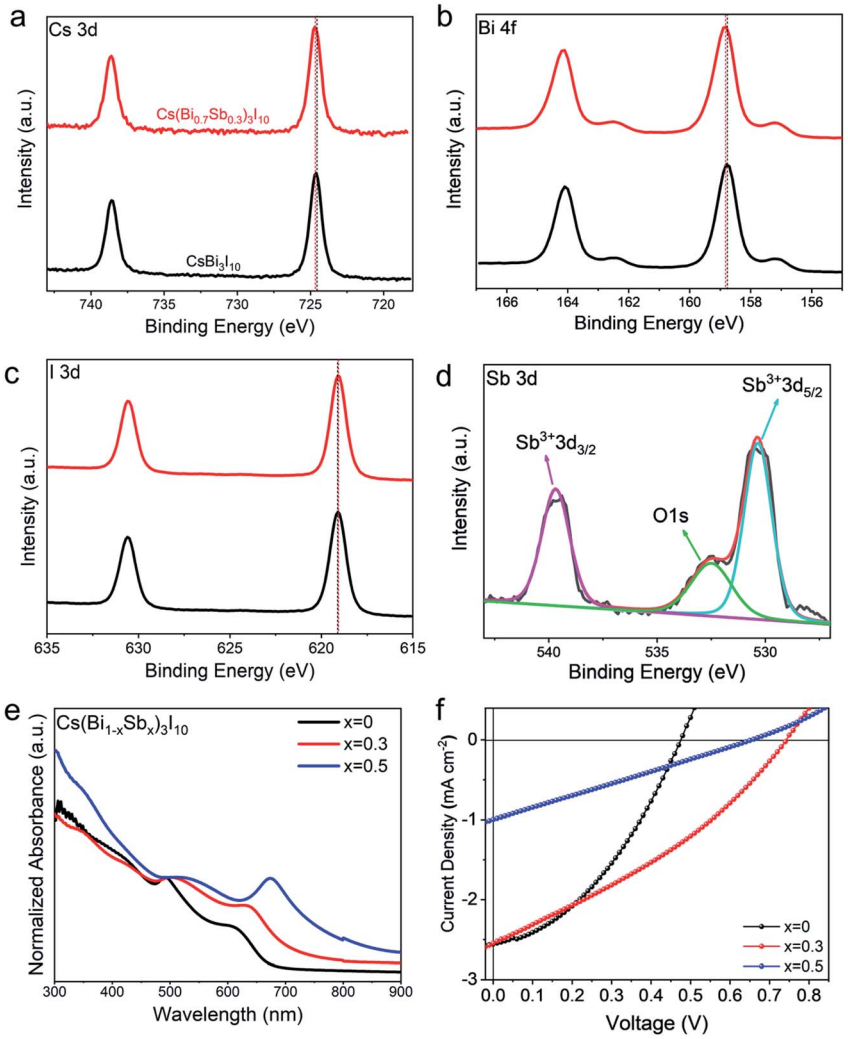

Fig. 2 XPS spectra of (a) Cs 3d, (b) Bi 4f, and (c) I 3d of CBI and CBSI-3 films, and (d) Sb 3d of CBSI-3 film. (e) UV-vis spectra of CBI, CBSI-3, and CBSI-5 films on the ITO/PEDOT substrate. (f) J–V curves of CBI, CBSI-3, and CBSI-5 devices with an inverted device architecture (ITO/PEDOT/CSBI/PCBM/bathocuproine (BCP)/Ag) measured under illumination (AM 1.5G, 100 mW cm^{-2}). All films illustrated here are synthesized from DMF/DMSO mixed solvent with volume ratio of 9 : 1.

performance parameters of devices with different DMSO concentrations are summarized in Table S2.†

The Sb-substitution ratio in the CBSI film is further optimized by using pure (100 vol%) DMSO solvent for film preparation. As shown in Fig. 4a, the device based on the pristine CBI without Sb substitution yields a low PCE of 0.55% with a V_{oc} of 0.46 V, a J_{sc} of 2.89 mA cm^{-2}, and a FF of 41.8%. All of the devices based on the Sb-substituted CBSI films reveal the increased V_{oc} (Table S3†), firstly increasing with the increasing of Sb-substitution ($x = 0.1$ to 0.3), then reaching a steady point ($x = 0.3$ to 0.4). The device based on CBSI-3 film with 30 mol% Sb substitution affords the best performance with a highest PCE of 1.06% and J_{sc} of 4.62 mA cm^{-2} as discussed in the above section. As illustrated in Fig. S13,† external quantum efficiency (EQE) curves of devices with different Sb contents were measured to confirm the highest J_{sc} of CBSI-3. In addition, the effect of CBSI-3 precursor solution concentration and post-treatment temperature on the photovoltaic performance is studied (Fig. S14 and S15†). The optimized concentration and thermal annealing temperature are 0.31 M and 100 °C, respectively, which gives the CBSI-3/PCBM bulk-heterojunction active layer a thickness of ~150 nm (Fig. S16†). Thermal annealing temperature lower than 100 °C would lead to incomplete DMSO evaporation of CBSI-3 films and inferior performance as shown in Fig. S15.† All of the above-investigated devices adopt the most popular commercial PEDOT as hole-transport-layer (HTL). However, PEDOT possesses a low-lying highest occupied molecular orbital (HOMO) of −5.10 eV compared with that (−5.90 eV) of $CsBi_3I_{10}$.[24] This large band offset is not favourable for holes transfer from HOMO of $CsBi_3I_{10}$ to HOMO of PEDOT, causing charge recombination at the interfaces. The PTAA with a deeper-lying HOMO (−5.42 eV) was then employed as the HTL instead of PEDOT to reduce the energy barrier of holes transfer. The CBSI-3 films fabricated onto the ITO/PTAA substrates show similar morphologies compared with those onto the ITO/PEDOT substrates (Fig. S17†). Fig. 4b shows the cross-

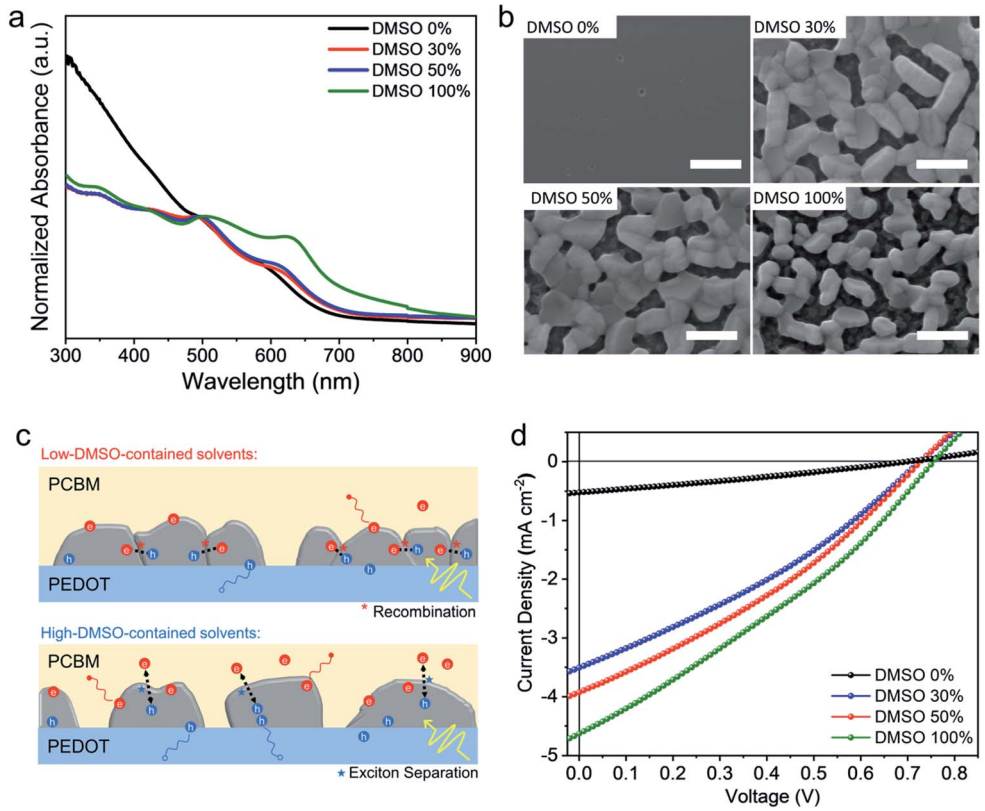

Fig. 3 (a) UV-vis spectra, (b) SEM images of CBSI-3 films synthesized from DMF/DMSO mixed solvents with different DMSO volume ratios. (c) Proposed exciton separation and charge transfer processes for CBSI-3 films synthesized from low- or high-DMSO-contained solvents. (d) The corresponding *J*–*V* curves of CBSI-3 based solar cells with the structure of ITO/PEDOT/CBSI-3/PCBM/BCP/Ag measured under illumination (AM 1.5G, 100 mW cm^{-2}).

sectional SEM image of the device based on the low-temperature processed p-i-n structure ITO/PTAA/CBSI-3/PCBM/BCP/Ag. The CBSI-3/PCBM active layer exhibits a typical bulk-heterojunction structure with PCBM permeating into the gaps surrounded by the CBSI-3 grains. As expected, the CBSI-3 solar cell using PTAA HTL outperforms that using PEDOT HTL, with a much improved V_{oc} (0.81 V *vs.* 0.75 V) and J_{sc} (5.47 mA cm^{-2} *vs.* 4.63 mA cm^{-2}) due to the better energy band alignment (Fig. 4c). As shown in Fig. 4d, the champion CBSI-3 solar cell shows a slight hysteresis and achieves a PCE of 1.54% with a V_{oc} of 0.81 V, J_{sc} of 5.47 mA cm^{-2} and FF of 34.8% under backward scanning with a scan step of 10 mV. To our best knowledge, this is the highest PCE among all of the reported AB_3X_{10} (A = MA^+, FA^+, and Cs^+; B= Bi^{3+} or Sb^{3+}; X= I^-, Cl^-) perovskite solar cells. The integrated J_{sc} from EQE spectrum for the champion solar cell is 5.21 mA cm^{-2}, which agrees well with the value of 5.47 mA cm^{-2} from the *J*–*V* plot (Fig. 4e). Fig. 4f shows the statistic variations of 40 devices based on the CBSI-3 films synthesized from the solvents with DMSO concentration of 70 vol%, 80 vol%, 90 vol%, and 100 vol% when using PTAA as HTL, and the results confirm the excellent reproducibility. Fig. S18† shows the performance tracking of the champion CBSI-3 solar cell obtained by continuous measuring the *J*–*V* curves under standard simulated illumination under ambient conditions, indicating that the device possesses superior stability, with the PCE keeping almost unchanged after 300s' continuous measurement. The storage and light-soaking stabilities of CBSI-3 solar cells were evaluated (Fig. S19 and S20†). The device can retain 95.1% and 90.2% of initial PCEs when stored in Ar atmosphere for 14 days and under continuous illumination for 7 days, respectively.

Conclusions

In summary, an ion substitution strategy has been adopted for the promising lead-free perovskite $CsBi_3I_{10}$ system to synthesize a series of $Cs(Bi_{1-x}Sb_x)_3I_{10}$ films (x = 0 to 0.5) for photovoltaic applications. After alloying the Sb^{3+} into the pristine $CsBi_3I_{10}$, the crystallization process has been obviously retarded, thus resulting in films with highly-crystalline large grains. The slowed-down crystallization rate might be caused by the coordination effect between Lewis acid Sb^{3+} and Lewis base DMSO, revealed by the solvent effect study. Meanwhile, the optical property has been improved after the Sb^{3+} incorporation, with the bandgap decreasing from 1.88 eV for $CsBi_3I_{10}$ to 1.66 eV for $Cs(Bi_{0.5}Sb_{0.5})_3I_{10}$ thin film. The specific Sb-substituted $CsBi_3I_{10}$ film morphology has formed a bulk-heterojunction structure with PCBM electron acceptor, facilitating the exciton separation. By using the PTAA as HTL, the optimal $Cs(Bi_{0.7}Sb_{0.3})_3I_{10}$ based solar cell achieves a champion PCE of 1.54% with

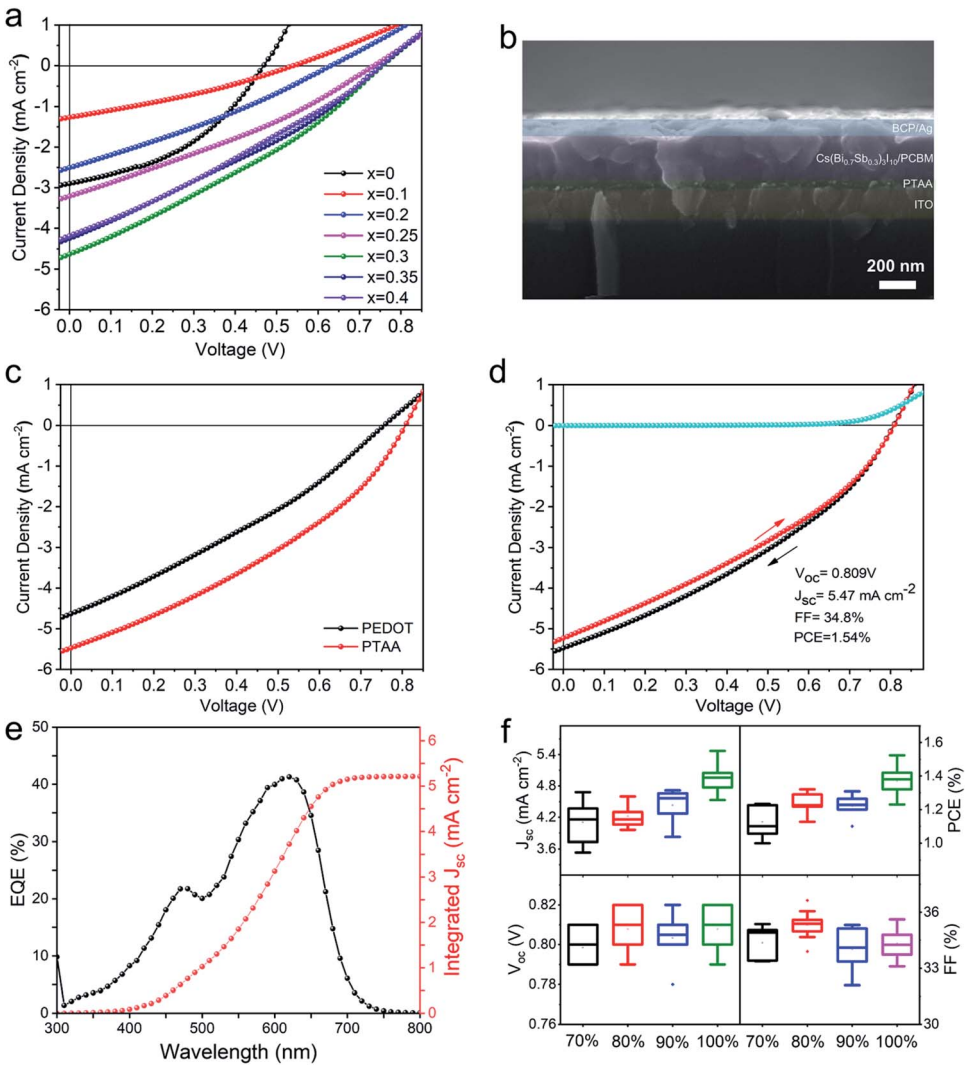

Fig. 4 (a) *J–V* curves of CBSI-based solar cells with different Sb substitution by using pure 100 vol% DMSO as the solvent. (b) Cross-sectional SEM image of the CBSI-3 solar cell by using PTAA as the HTL. (c) *J–V* curves of the CBSI-3 solar cells with PEDOT or PTAA as the HTL. (d) *J–V* and (e) EQE curves of the champion CBSI-3 solar cell. (f) Statistic variations of CBSI-3 devices fabricated by using solvents with different DMSO volume ratios.

excellent reproductivity, which is the highest record for the lead-free AB_3X_{10} system. This work provides an insight into manipulating the crystallization dynamics and enhancing the photovoltaic performance of Bi-based perovskite films.

Experimental section

Chemicals and materials

Indium tin oxide glasses (ITO, 15 Ω sq^{-1}) were purchased from South China Science & Technology Company Limited. Poly(3,4-ethylenedioxythiophene): polystyrene sulfonate (PEDOT, Clevios™ P VP AI 4083) aqueous dispersion and poly[bis(4-phenyl)(2,4,6-trimethylphenyl)amine (PTAA) were purchased from Ossila, UK. Cesium iodide (99.999% trace metals basis, Bismuth triiodide (BiI_3, 99%), Antimony triiodide (SbI_3, 99%), dimethylformamide (DMF, 99.8%), dimethylsulfoxide (DMSO, 99.9%), chlorobenzene (CB, 99.9% HPLC grade), bathocuproine (BCP, 96%), and isopropyl alcohol (IPA, 99.5%) were all purchased from Sigma-Aldrich. [6,6]-Phenyl-C61-butyric acid methyl ester (PCBM, 99%) was obtained from Xi'an Polymer Light Technology Corp.

Device fabrication

The patterned ITO glasses were ultrasonically cleaned sequentially by detergent, deionized water, acetone, and isopropanol and followed by an oxygen plasma (Tergeo Plasma Cleaner) treatment for 10 min. A 30 nm PEDOT layer was fabricated on the ITO substrate by spin-coating its aqueous dispersion under a rotation speed of 4000 rpm for 30 s, thermally annealed at 150 °C for 10 min in air. The resulted ITO/PEDOT is used as the substrate to support the active layer. As for PTAA substrates, 30 μL PTAA at a concentration of 10 mg mL^{-1} dissolved in CB was spin-coated in the ITO substrates at a speed of 4000 rpm for 35 s, and then annealed at 105 °C for 10 min. After cooling the

substrate to room temperature, it was prewetted with DMF before spin-coating the active layers. $Cs(Bi_xSb_{1-x})_3I_{10}$ coating solution was prepared by dissolving 0.31 M CsI, 0.93 M BiI_3 or SbI_3 according to the different molar ratios in DMSO or premixed solvents (DMF/DMSO) in the Ar-filled glovebox under constant stirring for 30 min at 50 °C, ready for use. $Cs(Bi_x-Sb_{1-x})_3I_{10}$ active layers were obtained by spin-coating at 5000 rpm from 30 s, and followed by thermal annealing at 100 °C for 10 min. The PCBM/CB solution was prepared by dissolving 20 mg of PCBM to 1 mL CB in an Ar-filled glovebox under constant stirring overnight at 50 °C. A 30 μL of PCBM/CB solution was deposited through spin-coating at 1500 rpm for 30 s. The BCP/IPA coating solution containing 0.80 mg mL^{-1} BCP was freshly prepared before use by dissolving 2.00 mg BCP to 2.50 mL IPA in an Ar-filled glovebox under constant stirring overnight at 50 °C. Next, 50 μL of BCP solution was spin-coated onto PCBM layer at 5000 rpm for 30 s. Each solution was filtered through a poly(tetrafluoroethylene) (PTFE) syringe filter (0.45 μm) before use. Finally, Ag electrode (100 nm in thickness) was deposited through a shadow mask under a high vacuum of $<5 \times 10^{-4}$ Pa. The effective area of the solar cells is 4.00 mm^2. All fabricated devices are stored in an Ar-filled glovebox before measurement.

Characterization

Scanning electron microscopy (SEM) images were carried out on a JSM-7100 hot field-emission SEM (JEOL, Japan). X-ray diffraction (XRD) patterns were obtained from a Burker X-ray Powder Diffractometer (D8 advanced eco) by scanning the angular range $10^\circ \leq 2\theta \leq 90^\circ$ using Cu Kα radiation ($\lambda = 1.5418$ Å). Absorption spectra were recorded on a UV-vis spectrophotometer (Cary 5000, Agilent Technologies). The steady-state PL emissions were measured at 450 nm light source excitation using a monochromatized Xe lamp, and the time-resolved photoluminescence (TRPL) decay studies were carried out with a 377 nm pulsed diode laser excitation source on a fluorescence spectrophotometer (FLSP-900, Edinburgh Instruments). The TRPL curves were fitted with a bi-exponential function of time (t):

$$F(t) = A_1 e^{-\frac{t}{\tau_1}} + A_2 e^{-\frac{t}{\tau_2}} + y_0$$

where A_1 and A_2 are prefactors while τ_1 and τ_2 represent the time constant, and y_0 is a constant.

Performance evaluation

The performance evaluation of the solar cell was done by using a Xenon-lamp-based solar simulator (Newport Oriel Solar 3A, AM 1.5G, 100 mW cm^{-2}). Solar simulator illumination intensity was determined by using a standard silicon cell (Oriel 91150V, 2 × 2 cm) calibrated by NREL. *J–V* curves were measured by using a computerized Keithley 2600 SourceMeter at a voltage scan step of 10 mV at the forward or reverse scanning direction. External quantum efficiency (EQE) measurements were done using an Oriel Quantum Efficiency Measurement Kit-QEPVSI (Newport) and data were collected by Oriel's TracQ™ Basic Software. A calibrated Si photodiode was used as a reference. Other than stability tests, all performance measurements were conducted in air under ambient conditions. The stability tests were performed in an Ar-filled glovebox, and the light source of 300 W Xenon lamp (300XF-22, newport) with 60 mW cm^{-2} power was employed for light-soaking stability.

Conflicts of interest

There are no conflicts to declare.

Acknowledgements

This work was financially supported by the Australian Research Council (ARC) Discovery Project, Griffith University Post-doctoral Fellowship (2017), the National Natural Science Foundation of China (52102197), and the CAS/SAFEA International Partnership Program for Creative Research Teams of Chinese Academy of Sciences, China.

References

1 A. Kojima, K. Teshima, Y. Shirai and T. Miyasaka, *J. Am. Chem. Soc.*, 2009, **131**, 6050–6051.
2 S. C. Warren, K. Voitchovsky, H. Dotan, C. M. Leroy, M. Cornuz, F. Stellacci, C. Hebert, A. Rothschild and M. Gratzel, *Nat. Mater.*, 2013, **12**, 842–849.
3 F. Hao, C. C. Stoumpos, D. H. Cao, R. P. H. Chang and M. G. Kanatzidis, *Nat. Photonics*, 2014, **8**, 489–494.
4 A. M. Ganose, C. N. Savory and D. O. Scanlon, *Chem. Commun.*, 2016, **53**, 20–44.
5 B. W. Park, B. Philippe, X. Zhang, H. Rensmo, G. Boschloo and E. M. Johansson, *Adv. Mater.*, 2015, **27**, 6806–6813.
6 B. Saparov, F. Hong, J.-P. Sun, H.-S. Duan, W. Meng, S. Cameron, I. G. Hill, Y. Yan and D. B. Mitzi, *Chem. Mater.*, 2015, **27**, 5622–5632.
7 F. Hao, C. C. Stoumpos, P. Guo, N. Zhou, T. J. Marks, R. P. Chang and M. G. Kanatzidis, *J. Am. Chem. Soc.*, 2015, **137**, 11445–11452.
8 P. P. Sun, Q. S. Li, L. N. Yang and Z. S. Li, *Nanoscale*, 2016, **8**, 1503–1512.
9 C. Zuo and L. Ding, *Angew. Chem., Int. Ed.*, 2017, **56**, 6528–6532.
10 Z. Jin, Z. Zhang, J. Xiu, H. Song, T. Gatti and Z. He, *J. Mater. Chem. A*, 2020, **8**, 16166–16188.
11 S. H. Reddy, R. R. Sumukam and B. Murali, *J. Mater. Chem. A*, 2020, **8**, 12951–12963.
12 C. Wu, Q. Zhang, G. Liu, Z. Zhang, D. Wang, B. Qu, Z. Chen and L. Xiao, *Adv. Energy Mater.*, 2019, **10**, 1902496.
13 Z. Xiao, Z. Song and Y. Yan, *Adv. Mater.*, 2019, **31**, 1803792.
14 Z. Xiao, W. Meng, J. Wang, D. B. Mitzi and Y. Yan, *Mater. Horiz.*, 2017, **4**, 206–216.
15 M. B. Johansson, H. Zhu and E. M. Johansson, *J. Phys. Chem. Lett.*, 2016, **7**, 3467–3471.
16 P. Sebastia-Luna, M. C. Gélvez-Rueda, C. Dreessen, M. Sessolo, F. C. Grozema, F. Palazon and H. J. Bolink, *J. Mater. Chem. A*, 2020, **8**, 15670–15674.

17 S. Ahmmed, M. A. Karim, M. H. Rahman, A. Aktar, M. R. Islam, A. Islam and A. B. Md. Ismail, *Sol. Energy*, 2021, **226**, 54–63.
18 J. Shin, M. Kim, S. Jung, C. S. Kim, J. Park, A. Song, K.-B. Chung, S.-H. Jin, J. H. Lee and M. Song, *Nano Res.*, 2018, **11**, 6283–6293.
19 D. B. Khadka, Y. Shirai, M. Yanagida and K. Miyano, *J. Mater. Chem. C*, 2019, **7**, 8335–8343.
20 G.-X. Liang, X.-Y. Chen, Z.-H. Chen, H.-B. Lan, Z.-H. Zheng, P. Fan, X.-Q. Tian, J.-Y. Duan, Y.-D. Wei and Z.-H. Su, *J. Phys. Chem. C*, 2019, **123**, 27423–27428.
21 P. Mariyappan, T. H. Chowdhury, S. Subashchandran, I. Bedja, H. M. Ghaithan and A. Islam, *Sustainable Energy Fuels*, 2020, **4**, 5042–5049.
22 J. Deng, L. Yang, X. Zhang, K. Wei, G. Du, G. Zhu and J. Zhang, *J. Mater. Chem. A*, 2022, **10**, 9384–9382.
23 H. Zhu, M. B. Johansson and E. M. Johansson, *ChemSusChem*, 2018, **11**, 1114–1120.
24 P. Mariyappan, T. H. Chowdhury, S. Subashchandran, I. Bedja, H. M. Ghaithan and A. Islam, *Adv. Mater. Interfaces*, 2021, **8**, 2002083.
25 H. Zhu, M. B. Johansson and E. M. J. Johansson, *ChemSusChem*, 2018, **11**, 1114–1120.
26 H. Lan, X. Chen, P. Fan and G. Liang, *J. Mater. Sci. Mater.*, 2021, 11183–11192.
27 S. Chatterjee and A. J. Pal, *J. Mater. Chem. A*, 2018, **6**, 3793–3823.
28 N. Li, Z. Zhu, J. Li, A. K. Y. Jen and L. Wang, *Adv. Energy Mater.*, 2018, **8**, 1800525.
29 F. Lyu, X. Zheng, Y. Wang, R. Shi, J. Yang, Z. Li, J. Yu and B.-L. Lin, *J. Mater. Chem. A*, 2019, **7**, 15627–15632.
30 C. H. Lu, G. V. Biesold-McGee, Y. Liu, Z. Kang and Z. Lin, *Chem. Soc. Rev.*, 2020, **49**, 4953–5007.
31 J. Liang, Z. Liu, L. Qiu, Z. Hawash, L. Meng, Z. Wu, Y. Jiang, L. K. Ono and Y. Qi, *Adv. Energy Mater.*, 2018, **8**, 1800504.
32 B. Yoo, A. Aziz, D. Ghosh, H. Park, G. Min, M. S. Islam and S. A. Haque, *J. Phys. Chem. C*, 2021, **125**, 8938–8946.
33 H. Han, M. Hong, S. S. Gokhale, S. B. Sinnott, K. Jordan, J. E. Baciak and J. C. Nino, *J. Phys. Chem. C*, 2014, **118**, 3244–3250.
34 N. Pai, J. Lu, M. Wang, A. S. R. Chesman, A. Seeber, P. V. Cherepanov, D. C. Senevirathna, T. R. Gengenbach, N. V. Medhekar, P. C. Andrews, U. Bach and A. N. Simonov, *J. Mater. Chem. A*, 2020, **8**, 2008–2020.
35 F. Hao, C. C. Stoumpos, R. P. Chang and M. G. Kanatzidis, *J. Am. Chem. Soc.*, 2014, **136**, 8094–8099.
36 S. Shahbazi, C.-M. Tsai, S. Narra, C.-Y. Wang, H.-S. Shiu, S. Afshar, N. Taghavinia and E. W.-G. Diau, *J. Phys. Chem. C*, 2017, **121**, 3673–3679.
37 C. Zhang, Y. Wang, X. Lin, T. Wu, Q. Han, Y. Zhang and L. Han, *J. Mater. Chem. A*, 2021, **9**, 1372–1394.
38 Q. Jia, C. Li, W. Tian, M. B. Johansson, E. M. J. Johansson and R. Yang, *ACS Appl. Mater. Interfaces*, 2020, **12**, 43876–43884.
39 M.-C. Tang, D. Barrit, R. Munir, R. Li, J. M. Barbé, D.-M. Smilgies, S. Del Gobbo, T. D. Anthopoulos and A. Amassian, *Sol. RRL*, 2019, **3**, 1800305.
40 A. Singh, S. Najman, A. Mohapatra, Y. J. Lu, C. Hanmandlu, C. W. Pao, Y. F. Chen, C. S. Lai and C. W. Chu, *ACS Appl. Mater. Interfaces*, 2020, **12**, 32649–32657.
41 T. C. Sum and N. Mathews, *Energy Environ. Sci.*, 2014, **7**, 2518–2534.
42 J. Kang, S. Chen, X. Zhao, H. Yin, W. Zhang, M. Al-Mamun, P. Liu, Y. Wang and H. Zhao, *Nano Energy*, 2020, **73**, 104799.
43 G. Chen, P. Wang, Y. Wu, Q. Zhang, Q. Wu, Z. Wang, Z. Zheng, Y. Liu, Y. Dai and B. Huang, *Adv. Mater.*, 2020, **32**, 2001344.
44 S. Chatterjee and A. J. Pal, *ACS Appl. Mater. Interfaces*, 2018, **10**, 35194–35205.
45 J. C. Hamill, J. Schwartz and Y.-L. Loo, *ACS Energy Lett.*, 2017, **3**, 92–97.
46 U. H. Hamdeh, R. D. Nelson, B. J. Ryan and M. G. Panthani, *J. Phys. Chem. C*, 2019, **123**, 13394–13400.